Application of Deep Learning to Estimate Atmospheric Gravity Wave Parameters in Reanalysis Datasets

D. Matsuoka[1, 2, 3], S. Watanabe[1], K. Sato[4], S. Kawazoe[5], W. Yu[3], and S. Easterbrook[3]

[1]Japan Agency for Marine-Earth Science and Technology (JAMSTEC), Yokohama, Japan.

[2]Japan Science and Technology Agency (JST), Kawaguchi, Japan.

[3]Department of Computer Science, University of Toronto, Toronto, Canada.

[4]Department of Earth and Planetary Science, University of Tokyo, Tokyo, Japan.

[5]Department of Earth and Planetary Sciences, Hokkaido University, Sapporo, Japan.

Corresponding author: Daisuke Matsuoka (daisuke@jamstec.go.jp)

Key Points:

- A deep learning approach was proposed to estimate the parameters of orographic gravity waves using 29-year reanalysis data.
- Gravity wave momentum fluxes at 100 hPa were directly converted from lower atmospheric data with a spatial resolution of 60 km.
- Using the proposed method, the maximum amplitudes of the strong momentum flux in the target area could be estimated quite well.

Abstract

Gravity waves play an essential role in driving and maintaining global circulation. To understand their contribution in the atmosphere, the accurate reproduction of their distribution is important. Thus, a deep learning approach for the estimation of gravity wave momentum fluxes was proposed, and its performance at 100 hPa was tested using data from low resolution zonal and meridional winds, temperature, and specific humidity at 300, 700, and 850 hPa in the Hokkaido region (Japan). To this end, a deep convolutional neural network was trained on 29-year reanalysis datasets (JRA-55 and DSJRA-55), and the final 5-year data were reserved for evaluation. The results showed that compared to ground truth data, the fine-scale momentum flux distribution of the gravity waves could be estimated at a low computational cost. Particularly, in winter, when gravity waves are stronger, the median RMSE of the maximum momentum flux in the target area was 0.06–0.13 mPa.

Plain Language Summary

Deep learning has been proven to be a powerful tool in the atmospheric sciences and weather and climate prediction applications. In this study, it is used to obtain physical parameters of fine-scale mountain waves in the lower stratosphere (~18km), which drive global circulations in the middle atmosphere (10–100km), based on large-scale low-level (1–9km) atmospheric flows, temperature, and humidity. By training a convolutional neural network using 29-year atmospheric reanalysis dataset, the large-scale inputs are well down-scaled into the fine-scale wave parameters, significantly saving computational costs of weather and climate predictions.

1 Introduction

Atmospheric gravity waves are small-scale waves that originate from different sources, including high mountains, jet-front systems, and convection. They propagate momentum vertically and play an important role in driving and maintaining general circulation in the stratosphere and mesosphere (Fritts and Alexander, 2003). Thus, it is essential to quantitatively evaluate their contribution when estimating momentum fluxes. Since the 1980s, with the advancements in meteorological observations and numerical modeling, a great deal of studies related to gravity waves have been conducted, and theoretical advances in understanding them have been achieved (Tsuda et al., 1990; Sato, 1994; Hertzog et al., 2008; Wright et al., 2017; Ern et al., 2008; Alexander et al., 1995; Chun and Baik, 1998; Sato et al., 2009; Sato et al., 2012; Geller et al., 2013; Plougonven et al., 2013; Laura et al., 2017; Plougonven and Zhang, 2014).

The spatial scales of gravity waves are smaller than the resolution of typical atmospheric models, most of which capture the effects of sub-grid-scale gravity waves by parameterizing them in the computational grid (Palmar et al., 1986; Alexander et al. 2010). To directly simulate the propagation of gravity waves without parameterization, Watanabe et al. (2008) developed an atmospheric general circulation model that is characterized by a fine vertical resolution. The gravity wave-resolving model showed superior accuracy; however, it was associated with high computational costs. Therefore, new low-cost statistical methods for the estimation of sub-grid-scale gravity wave momentum fluxes, which are based on grid-scale meteorological elements, are needed to perform long-term integration at global scales (Bushell et al., 2015).

Recently, image pattern recognition using deep learning has attracted a lot of attention in various fields (Krizhevsky et al., 2012). Deep learning, which uses multi-layered neural networks to learn image features from large amounts of data, has demonstrated high performance in a

variety of tasks, including image transformation, in which an input image is transformed into another image. In the field of atmospheric science, deep learning techniques have also been used in tropical cyclone and atmospheric river detection (Kurth et al., 2018), stationary front detection (Matsuoka et al., 2019), precipitation bias correction (Tao et al., 2016), and ozone dry deposition velocity parameterization (Silva et al., 2019). Particularly, Shilva et al. (2019) used deep neural networks to estimate sub-grid processes, rendering the computational process 10 times faster. Deep learning has the advantage that once an estimation model has been built using the training dataset, the computational cost associated with running the model on further data is much lower than that associated with directly resolving the sub-grid scale process.

Therefore, the aim of this study was to perform a low-computational-cost estimation of the momentum fluxes associated with the fine-scale gravity waves in the lower stratosphere based on the lower resolution data in the troposphere using deep learning techniques that are based on a statistical downscaling method. Additionally, the preliminary momentum flux estimation results due to the orographic gravity waves over the Hokkaido region in Japan were also described.

2 Data and Methods

2.1 Reanalysis data and training data preparation

Our model could learn the relationship between coarse-resolution atmospheric fields and high-resolution wind fluxes. As input, the Japanese 55-year Reanalysis (JRA-55) (Kobayashi et al., 2015; Harada et al., 2016), which is a global reanalysis data, was used, and for output (ground truth), the corresponding regional downscaling data (DSJRA-55) (Kayaba, 2016), provided by the Japan Meteorological Agency (JMA), was used (JRA-55 and DSJRA-55 had horizontal resolutions of ∼60 and 5 km, respectively).

The lower resolution (60 km) physical quantities used as input data were the zonal wind (u), meridional wind (v), air temperature (T), and specific humidity (q) at 300, 700 and 850 hPa of JRA-55 as shown in Figures 1a–1l. The finer resolution (5 km) orography of DSJRA-55 was also used as input data; thus, the total number of input channels was 13. As the fine scale (5 km) ground truth corresponding to the input data, 3-D wind fluctuations (u', v', and w') with horizontal scales approximately less than 1000 km at 100 hPa of DSJRA-55 as shown in Figures 1m–1p were used.

The analysis domain was a rectangular area (∼1,000 km × 1,000 km), which included the Hidaka Mountains as shown in Figure 1m. The DSJRA-55 data was cut out into 128 × 128 uniform grids to fit its grid system, and to better facilitate the deep learning process, the JRA-55 data was converted into the same grids using bicubic interpolation.

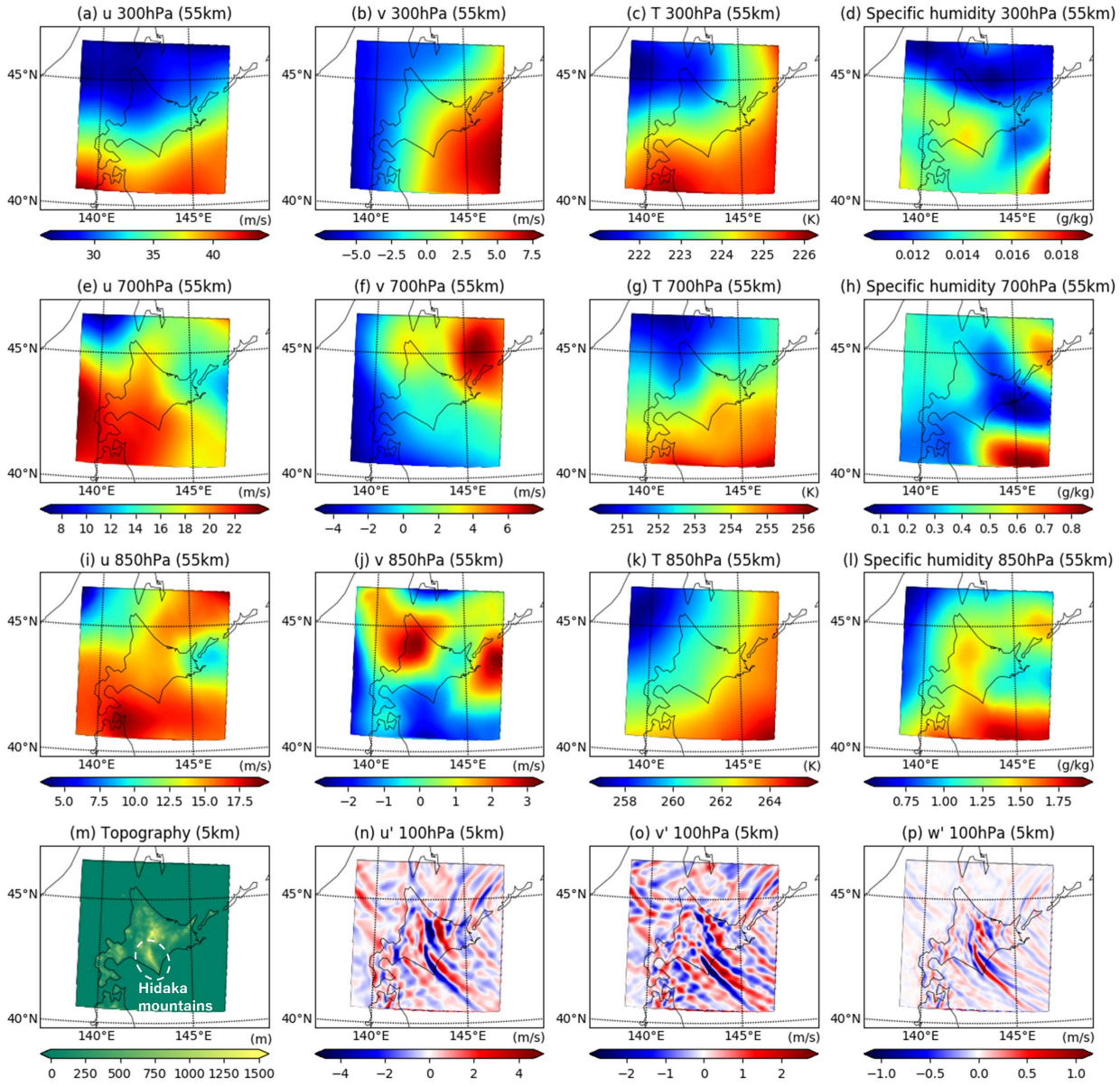

Figure 1. **(a)**–**(m)** Input data and **(n)**–**(p)** Ground truth of output data for the deep convolutional neural network.

2.2 Deep convolutional neural network

Using the dataset described above, our model was designed to learn the transformation of the physical quantities in the troposphere (300, 700, and 850 hPa) to the small-scale 3-D wind fluctuations (u', v' and w') in the lower stratosphere (100 hPa). The training for each of u', v', and w' was done independently. Additionally, to convert the input data to the corresponding output data, a U-Net convolutional neural network which was originally designed for image segmentation/partitioning tasks, was used (Ronneberger et al., 2015). In the U-Net, the model was automatically trained to learn the relationship between the input data and the corresponding output data using a contracting path to capture the context information for each image and a symmetric expansive path to enable precise localization as shown in Figure 2. The contracting

path was composed of convolutional operations that captured local features (feature maps) using 3 × 3 convolutional filters ("Conv 3×3", dark blue arrows in Figure 2) and downsampling operations that reduce the size of each feature map using 2 × 2 pooling filters ("Max pool 2×2", red arrows in Figure 2). The expansive path consisted of the deconvolutional operation, which used the convolutional filters and upsampling operations to recover the size of the feature maps with the help of unpooling filters ("Up-conv 2 × 2", green arrows in Figure 2). Additionally, the context information from the contracting path was combined with the location information in the expansive path using skip-connections ("copy and crop", grey arrows in Figure 2). At the end of the operation, the output value of each grid was calculated using the convolutional filters ("Conv 1 × 1", cyan arrow in Figure 2). The hyper parameter settings such as the number of layers and filters, as well as the filter size were the same as those reported by Matsuoka et al. (2019).

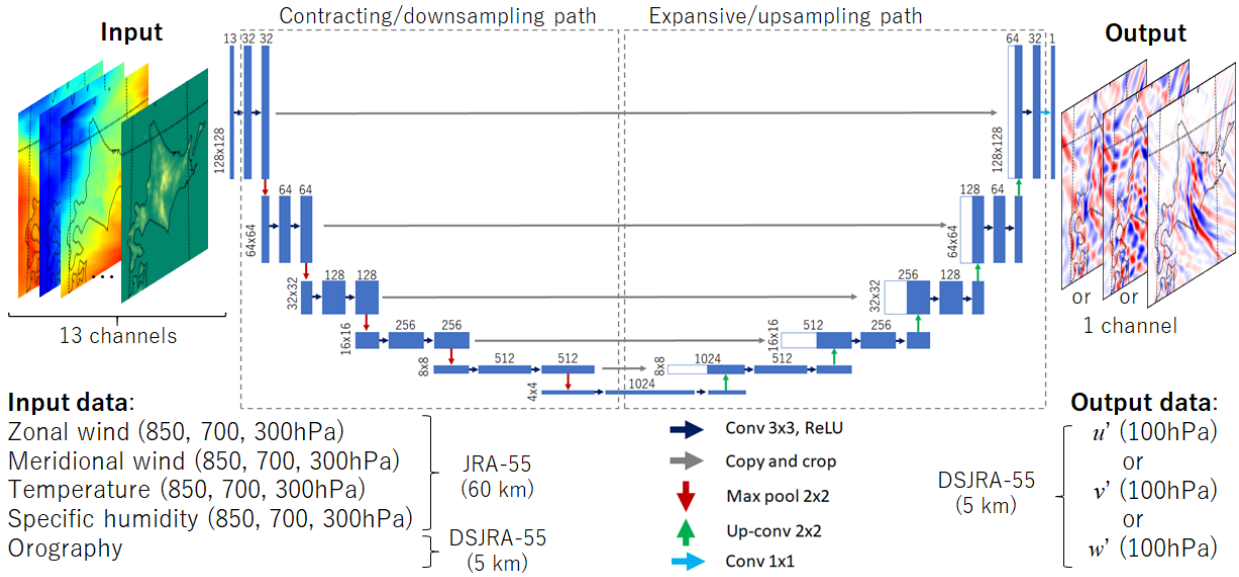

Figure 2. U-net architecture. The multi-channel feature maps in each layer are represented using blue boxes. The number of channels and the sizes of the feature maps are listed on top and left of the box. Each operation is illustrated using arrows.

As with general supervised machine learning, our method consisted of a training and validation phase for model fitting, and an estimation phase for performance measurement. For the training and validation, 29-year JRA-55 and DSJRA-55 data (time interval, 6 h; total time step, 42,364) from the 1979–2007 period was used, and for the performance tests, 5-year data (7,308 steps) from the 2008–2012 period was used. During the training and validation phase, the error between the output from the U-Net and the ground truth (previously stated as the correct output data) was measured, and the model was repeatedly optimized using this training data until its predictive error on the validation data converged to a certain threshold. Here, the error function (called the loss function) was defined using the Tanimoto coefficient (Tanimoto, 1958), which represents the similarity between the two groups, as follows:

$$Tanimoto\ coefficient\ error = 1 - y \cdot \hat{y}/(y^2 + \hat{y}^2 - y \cdot \hat{y}) \qquad (1),$$

where $y \cdot \hat{y} = \sum_i y_i \hat{y}_i$, $y^2 = \sum_i y_i^2$, and $\hat{y}^2 = \sum_i \hat{y}_i^2$. Here, y_i and $\hat{y}_i$ represent the target physical quantities, such as u', v' and w', of the i-th grid in ground truth and output of the validation data, respectively. The Tanimoto coefficient error is usually applicable when the values concerned are

positive, and it ranges from 0 to 1. However, its application can also be extended to negative values without any contradiction. Additionally, it may exceed 1, when the signs of the estimated value and the ground truth are different. After the training and validation phase, the reserved test data were then fed into the trained U-Net for the evaluation phase.

The source code for deep learning was implemented in Python 3.6.3 using Keras (TensorFlow 2.1 backend) (Chollet, 2015), which runs on an NVIDIA DGX station with four Tesla V100 graphical processing units (GPUs). The training of the 29-year data over one epoch lasted ~89 s, and the number of iterations of the training for u', v', and w' that were required to converge the errors were 33, 46 and 93, respectively, and their errors with respect to the test data were 0.764, 0.835 and 0.696, respectively.

3 Results and Discussion

In this section, the results of the evaluation of the test data for a period of over five years are presented and discussed. Primarily, as an example of the test, the results of the estimation obtained using the trained U-Net on the test data are shown in Figure 1 (11/22/2011 0:00:00 UTC) and described in Figure 3. The ground truth and estimation results for u', v', and w' are shown in Figures 1n–1p and Figures 3a–3c, respectively. Comparing the ground truth with the estimation results, u', v', and w' appeared to be qualitatively consistent on land and off the south coast. Particularly, the positive and negative stripes stretching from the Hidaka Mountains in central Hokkaido to the southeast were well reproduced in the estimation results. Conversely, the strong amplitudes of u' and v' were not well reproduced on the sea, except on the south side.

Secondly, the ground truth and estimation results of the momentum flux (i.e., the vertical flux of the zonal momentum, $\rho u'w'$; the vertical flux of the meridional momentum, $\rho v'w'$; and their vector fields) are shown in Figures 3d–3f and Figures 3g–3i, respectively. Here, the atmospheric density, ρ, at a pressure level of 100 hPa was 0.141515 kg m^{-3}. Similar to u', v' and w', the pattern of negative values extending from the Hidaka Mountains to the southeast also agreed well with the ground truth and estimation results. For the horizontal vectors, the regions with strong momentum fluxes and their directions (southwestward) appeared to coincide with each other, as seen on the southern side of the Hidaka Mountains.

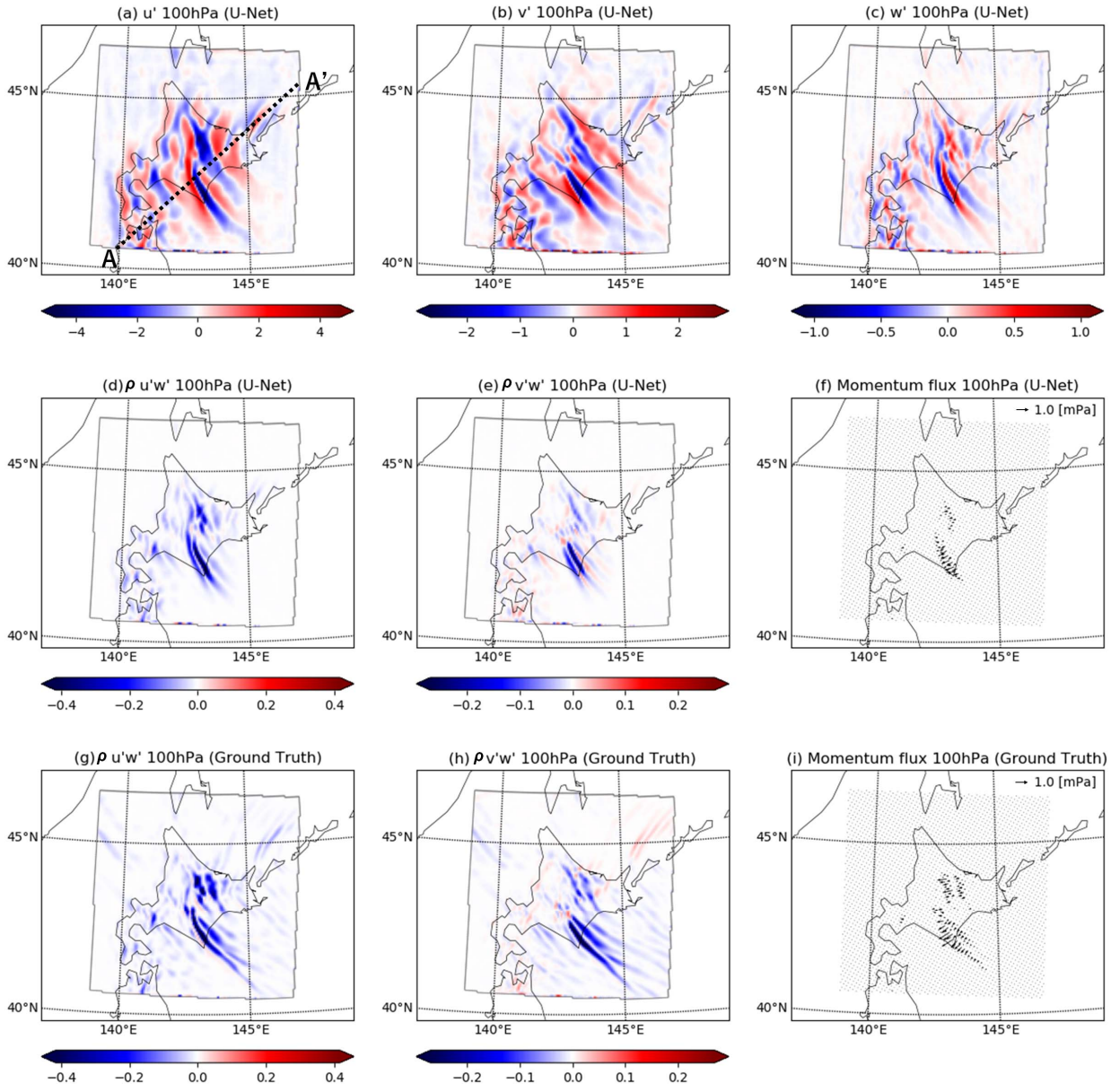

Figure 3. **(a)**–**(c)** Estimation results of u', v', and w'on 0:00:00 11/22/2011 UTC. Their ground truth are shown in Figures 1(n)–(p). **(d)**–**(f)** Estimation results of $\rho u'w'$, $\rho v'w'$, and their vector fields, and **(g)**–**(i)** their corresponding ground truth.

Figure 4 shows the plot of each component in the direction orthogonal to the strong wave vector seen on the southeast side of the analysis region. The location of the A–A' direction is depicted as the black dotted line in Figure 3(a). For u', v', and w', the shape of the fine-scale waves appeared to be consistent with the ground truth and the estimation results, meaning that the estimation of both the wave strength and the downscaling from the 60 km mesh data to the 5 km data were appropriately performed using the U-Net. Particularly, the maximum amplitudes of the estimation results of u', v', and w' along the A–A' direction were –5.46, –3.20, and 1.05 m s^{-1}, while their ground truth were –4.58, –4.02, and 1.17 m s^{-1}, respectively. Additionally, the

location of the maximum amplitudes corresponding to v' were slightly shifted, and coincided quite well with those corresponding to u' and w'.

Generally, as shown in Figures 4d and 4e, the momentum fluxes between the ground truth and the estimation results corresponded well. Additionally, the estimation results of the maximum amplitude of the vertical flux of the zonal and meridional momentum were –0.83 and –0.49 mPa, while their ground truth were –0.78 and –0.39 mPa, respectively. The maximum momentum flux magnitude was 0.87 mPa for the estimation result and 0.93 mPa for the ground truth. The peak of the maximum amplitude corresponding to v' was out of phase compared with those of the maximum amplitudes corresponding to u' and w', and this led to an underestimation of the maximum momentum flux magnitude obtained by multiplying them.

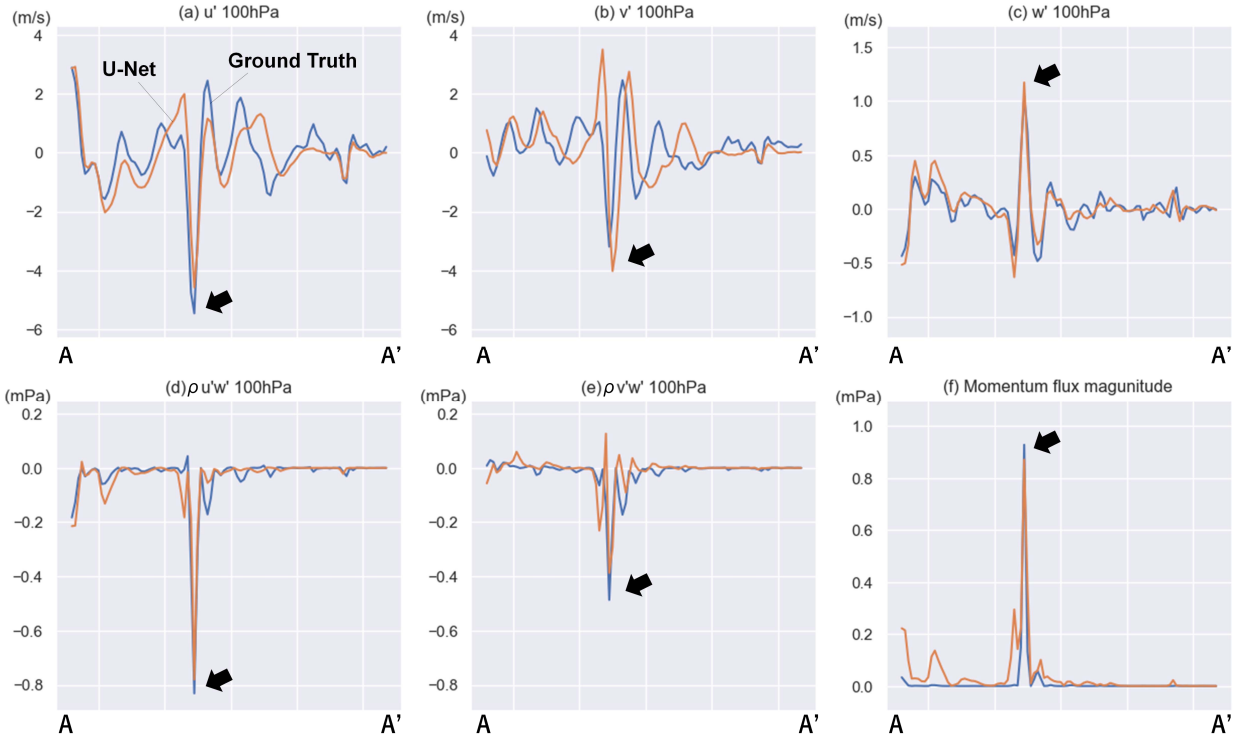

Figure 4. Comparison of the magnitude of the amplitude of the gravity waves based on the estimation results and the ground truth along the A–A' direction shown in Figure 3a. **(a)** u', **(b)** v', **(c)** w', **(d)** $\rho v'w'$, **(e)** $\rho v'w'$, and **(f)** momentum flux magnitude.

Finally, the estimation results of the maximum momentum flux in the target area for each month was demonstrated. Figures 5a–5c depict the distribution of the ground truth, the estimated values of the momentum flux magnitude, and the zonal and meridional momentum vertical fluxes, respectively, as monthly box plots. The magnitude of the momentum flux, including the zonal and meridional components, tended to be larger in winter and smaller in summer. This could possibly be attributed to the jet stream that moves southward to the analysis area in winter; hence, the wind close to the surface is more frequently strongly sufficient to excite orographic gravity waves. This seasonal change trend was consistent with the estimated values as well as the ground truth. Additionally, the variation in the estimation results for each month was approximately consistent with the ground truth, and the maximum and 3rd quartile were in good agreement, especially during the season of strong gravity waves (October–April). For the median

in December, when the momentum fluxes are strongest, the estimated values of the magnitude, $\rho u'w'$, and $\rho v'w'$ were 0.37, 0.33, and 0.14 mPa, respectively, and their corresponding ground truth values were 0.28, 0.25, and 0.09 mPa, respectively. The median values in the estimation results were below those of the ground truth for most months, especially in the winter months. This could be attributed to the misalignment of the phases between u', v', and w' in the estimation results, as mentioned above.

Furthermore, the estimation errors (RMSE: Root Means Squared Error) for the momentum flux magnitude, the vertical fluxes of the zonal and the meridional momentum are shown in Figures 5d–5f, respectively. The RMSE, in terms of the magnitude, zonal, and meridional components, was large in winter and small in summer, corresponding to the magnitude of the gravity wave. The median, 3rd quartile, and maximum of the estimation errors in December were approximately 0.13, 0.32, and 0.70 mPa, respectively. The series of results presented in this section show that the proposed method can adequately estimate orographic gravity waves in each season.

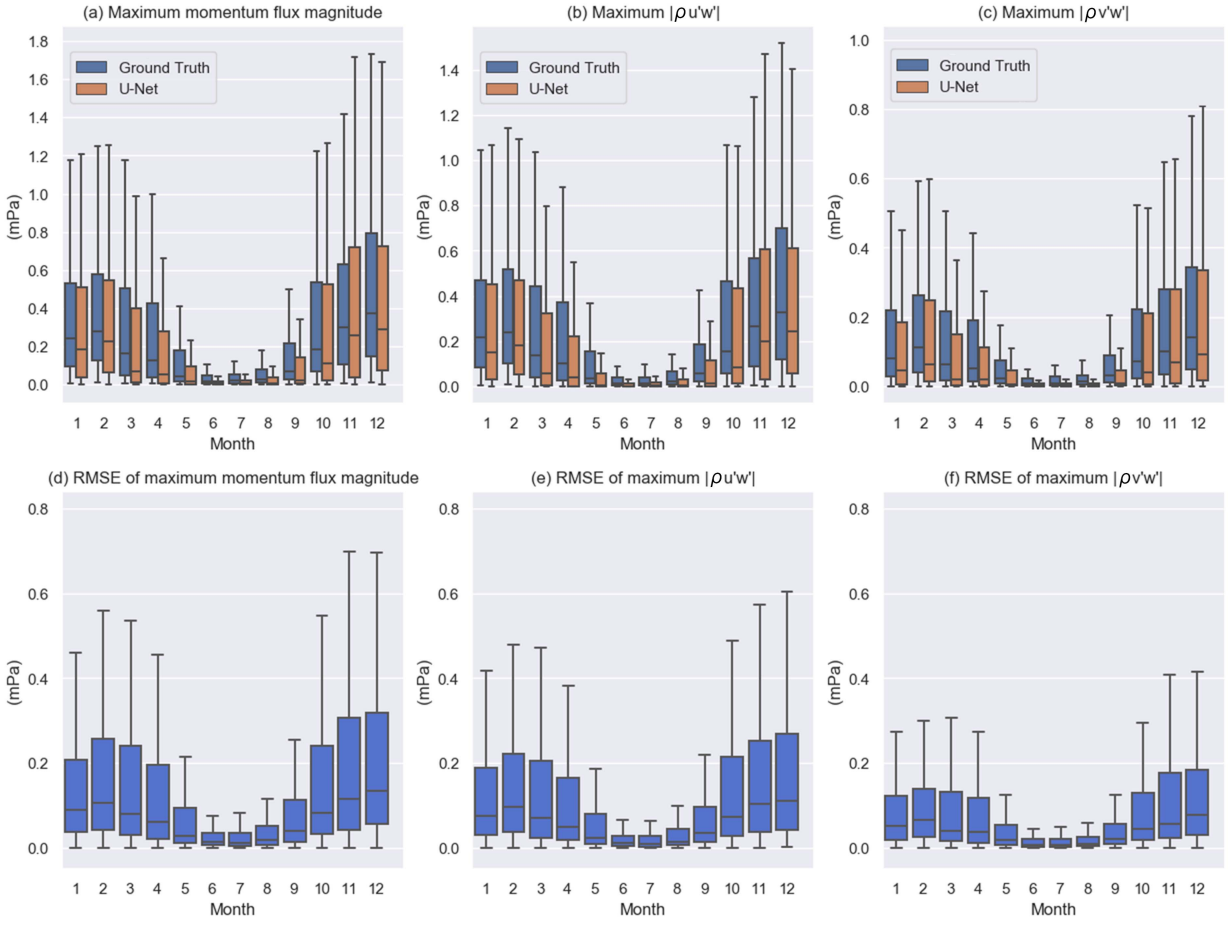

Figure 5. Monthly changes in the estimated maximum momentum flux in the target area. Estimation results and ground truth for **(a)** Momentum flux magnitude, **(b)** $\rho u'w'$, and **(c)** $\rho v'w'$, and **(e)**–**(f)** their estimation errors (RMSEs).

4 Conclusions

In this study, a deep convolutional deep neural network was used to estimate the parameters of orographic gravity waves. Low-resolution data (u, v, T, and q) at pressure levels of 850, 700, and 300 hPa in the troposphere as well as high-resolution orographic data were directly transferred to the 3-D wind fluctuations (u', v', and w') in the lower stratosphere. Particularly, in winter, parameters such as the maximum amplitude of the strong momentum flux could be estimated.

On the other hand, generally, machine learning techniques vary greatly in the quality of the results they produce depending on the neural network layer setting, the choice of the training data, and the definition of the error function. Therefore, it is necessary to optimize the learning method taking into account the area to which it would be applied, the season, as well as the parameters to be extracted.

One of the advantages of the proposed method is the low computational cost associated with its application on untrained data. By adopting the proposed method in a global atmospheric model, the realization of long-term integrations that incorporate the effects of gravity waves will be possible. Such deep learning-based methods can be particularly useful in the parameterization of non-orographic gravity waves, which often have multiple origins and have generation mechanisms that are still unclear. Therefore, to apply this proposed method to non-orographic gravity waves, further studies are still needed.

Acknowledgments, Samples, and Data

This work was supported by the Japan Science and Technology Agency (JST), PRESTO (Grant Number JPMJPR1777) and JST, CREST (Grant Number JPMJCR1663). JRA-55 and DSJRA-55 datasets were obtained from https://jra.kishou.go.jp/JRA-55/index_en.html, and https://jra.kishou.go.jp/DSJRA-55/index_en.html, respectively.

References

Alexander, M. J., Holton, J. R., & Durran, D. R. (1995), The gravity wave response above deep convection in a squall line simulation. *J. Atmos. Sci.*, *52*, 2212–2226. doi: 10.1175/1520-0469(1995)052<2212:TGWRAD>2.0.CO;2.

Alexander, M. J., Geller, M., McLandress, C., Polavarapu, S., Preusse, P., Sassi, F., Sato, K., Eckermann, S., Ern, M., Hertzog, A., Kawatani, Y., Pulido, M., Shaw, T. A., Sigmond, M., Vincent, R., & Watanabe, S. (2010), Recent developments in gravity-wave effects in climate models and the global distribution of gravity-wave momentum flux from observations and models. *Quart. J. Roy. Meteor. Soc.*, *136*, 1103–1124. doi:10.1002/qj.637.

Bushell, A.C., Butchart, N., Derbyshire, S. H., Jackson, D. R., Shutts, G. J., Vosper, S. B., & Webster, S. (2015), Parameterized gravity wave momentum fluxes from sources related to convection and large-scale precipitation processes in a global atmosphere model. *J. Atmos. Sci.*, 4349–4371. doi:10.1175/JAS-D-15-0022.1.

Chun, H. & Baik, J. (1998), Momentum flux by thermally induced internal gravity waves and its approximation for large-scale models. *J. Atmos. Sci.*, *55*, 3299–3310. doi:10.1175/1520-0469(1998).055<3299:MFBTII>2.0.CO;2.

Ern, M., Trinh, Q. T., Preusse, P., Gille, J. C., Mlynczak, M. G., Russell III, J. M., & Riese, M. (2018), GRACILE: a comprehensive climatology of atmospheric gravity wave parameters based on satellite limb soundings. *Earth Syst. Sci. Data*, *10*, 857–892. doi:10.5194/essd-10-857-2018.

Fritts, D. C., & Alexander, M. J. (2003), Gravity wave dynamics and effects in the middle atmosphere. *Rev. Geophys.*, *41*(1), 1003. doi:10.1029/2001RG000106.

Geller, M. A., Alexander, J. J., Love, P. T., Bacmeister, J., Ern, M., A., Hertzog, Manzini, E., Preusse, P., Sato, K., Scaife, A. A., & Zhou, T. (2013), A comparison between gravity wave momentum fluxes in observations and climate models. *J. Clim.*, *26*, 6383–6405. doi: 10.1175/JCLI-D-12-00545.1.

Harada, Y., Kamahori, H., Kobayashi, C., Endo, H., Kobayashi, S., Ota, Y., Onoda, H., Onogi, K., Miyaoka, K., & Takahashi, K. (2016), The JRA-55 Reanalysis: Representation of atmospheric circulation and climate variability. *J. Meteor. Soc. Japan*, *94*, 269–302. doi:10.2151/jmsj.2016-015.

Hertzog, A., Boccara, G., Vincent, R. A., Vial, F., & Cocquerez, P. (2008), Estimation of gravity wave momentum flux and phase speeds from quasi-Lagrangian stratospheric balloon flights. Part II: Results from the Vorcore campaign in Antarctica. *J. Atmos. Sci.*, *65*, 3056–3070. doi:10.1175/2008JAS2710.1.

Kayaba, N., Yamada, T., Hayashi, S., Onogi, K., Kobayashi, S., Yoshimoto, K., Kamiguchi, K., & K. Yamashita, (2016), Dynamical regional downscaling using the JRA-55 Reanalysis (DSJRA-55). *SOLA*, *12*, 1–5. doi:10.2151/sola.2016-001.

Kobayashi, S., Ota, Y., Harada, Y., Ebita, A., Moriya, M., Onoda, H., Onogi, K., Kamahori, H., Kobayashi, C., Endo, H., Miyaoka, K., & Takahashi, K. (2015), The JRA-55 Reanalysis: General specifications and basic characteristics. *J. Meteor. Soc. Japan*, *93*, 5–48. doi:10.2151/jmsj.2015-001.

Kurth, T., Treichler, S., Romero, J., Mudigonda, M., Luehr, N., Phillips, E., Mahesh, A., Matheson, M., Deslippe, J., Fatica, M., Prabhat, & Houston, M. (2018), Exascale deep learning for climate analytics. *Proc. Int. Conf. High Performance Compting, Networking, Storage, and Analysis (SC18)*. doi:10.1109/SC.2018.00054.

Krizhevsky, A., Sutskever, I., & Hinton, G. E., (2012), ImageNet classification with deep convolutional neural networks. *Adv. Neural Inf. Process. Syst.*, *25*, 1097–1105. doi:10.1145/3065386.

Matsuoka, D., Sugimoto, S., Nakagawa, Y., Kawahara, S., Araki, F., Onoue, Y., Iiyama, M., & Koyamada, K. (2019), Automatic detection of stationary fronts around Japan using a deep convolutional neural network. *SOLA*, *15*, 154–159. doi:10.2151/sola.2019-028.

Palmer, T. N., G. J. Shutts, and R. Swinbank (1986), Alleviation of a systematic westerly bias in general circulation and numerical weather prediction models through an orographic gravity wave drag parametrization. *Quart. J. Roy. Meteor. Soc.*, *112*, 1001–1039, doi: 10.1002/qj.49711247406.

Plougonven, R., & Zhang, F. (2014), Internal gravity waves from atmospheric jets and fronts. *Rev. Geophys.*, *52*, 33–76. doi:10.1002/2012RG000419.

Plougonven R, Hertzog, A., & Guez, L. (2013), Gravity waves over Antarctica and the Southern Ocean: consistent momentum fluxes in mesoscale simulations and stratospheric balloon observations. *Q. J. R. Meteorol. Soc.*, *139*, 101–118. doi:10.1002/qj.1965.

Ronneberger, O., Fischer, P., & Brox T., (2015), U-Net: Convolutional networks for biomedical image segmentation. *Lect. Notes Comput. Sci.*, *9351*, 234–241. doi:10.1007/978-3-319-24574-4_28.

Sato, K. (1994), A statistical study of the structure, saturation and sources of inertio-gravity waves in the lower stratosphere observed with the MU radar. *J. Atmos. Terr. Phys.*, *56*, 755–774.

Sato, K., Watanabe, S., Kawatani, Y., Tomikawa, Y., Miyazaki, K., & Takahashi, M. (2009), On the origins of mesospheric gravity waves. *Geo. Phys. Lett.*, *36*, L19801. doi:10.1029/2009GL039908.

Sato, K., Tateno, S., Watanabe, S., & Kawatani, Y. (2012), Gravity wave characteristics in the Southern Hemisphere revealed by a high-resolution middle-atmosphere general circulation model. *J. Atmos. Sci.*, *69*, 1378–1396. doi:10.1175/JAS-D-11-0101.1.

Tsuda, T., Murayama, Y., Yamamoto, M., Kato, S., & Fukao, S. (1990), Seasonal variation of momentum fluxes in the mesosphere observed with the MU radar. *Geophys. Res. Lett.*, *17*, 725–728.

Tao, Y., Gao, X., Hsu, K., & Sorooshian, S. (2016), A deep neural network modeling framework to reduce bias in satellite precipitation products. *J. Hydrol.*, *17*, 931–945. doi:10.1175/JHM-D-15-0075.1.

Tanimoto, T. T. (1958), An Elementary Mathematical Theory of Classification and Prediction. *International Business Machines Corporation*, 10.

Watanabe, S., Kawatani, Y., Tomikawa, Y., Miyazaki, K., Takahashi, M., & Sato, K. (2008), General aspects of a T213L256 middle atmosphere general circulation model. *J. Geophys. Res.*, *113*, D12110. doi:10.1029/2008JD010026.

Wright, C. J., Hindley, N. P., Hoffmann, L., Alexander, M. J., & Mitchell, N. J. (2017), Exploring gravity wave characteristics in 3-D using a novel S-transform technique: AIRS/Aqua measurements over the Southern Andes and Drake Passage. *Atmos. Chem. Phys.*, *17*, 8553–8575. doi:10.5194/acp-17-8553-2017.